Beam-Induced Damage to the Tevatron Collimators: Analysis and Dynamic Modeling of Beam Loss, Energy Deposition and Ablation[*]

A.I. Drozhdin, N.V. Mokhov, D.A. Still and R.V. Samulyak[†]

Fermi National Accelerator Laboratory

P.O. Box 500, Batavia, IL 60510, USA

[†] *BNL, Upton, NY 11973, USA*

June 1, 2004

Abstract

Thorough analysis is performed on beam-induced damage to components of the Tevatron superconducting collider occurred in December 2003. The damage was induced by a failure in the CDF Roman Pot detector positioning at the end of a 980×980 GeV proton-antiproton colliding beam store. Possible scenarios of this failure, including excessive halo generation and superconducting magnet quenching, are studied via realistic simulations using the STRUCT and MARS14 codes. It is shown that the interaction of a misbehaved proton beam with the collimators result in rapid local heating. A detailed consideration is given to the ablation process for the collimator material taking place in high vacuum. It is shown that ablation of the tungsten (primary collimator) and stainless steel (secondary collimator) jaws results in the creation of a groove in the jaw surface as observed after the December accident. Analysis and simulations performed show that we have a good understanding of the entire picture, both on dynamics and material damage sides. Calculated parameters of the grooves created in the collimators are very similar to those observed after the accident.

1   Introduction

There are 24 cryogenic refrigerator houses for the Fermilab Tevatron ring. One house cryogeniclly keeps about 40 magnets at superconductng temperatures. On December 5, 2003, the Tevatron suffered a 16 house quench during the end of a proton-antiproton colliding beam store and just before a Tevatron planned study period. This multiple house quench became significant due to the fact that in addition to the 16 house quenching, 2 collimators used for halo reduction at the CDF and DØ interaction points (IP) were damaged with beam. In addition, a cryogenic spool piece that houses correction elements was also damaged as a result of helium evaporation and pressure rise during the quench, requiring 10 days of Tevatron downtime for repairs.

The initial reason of the large quench was found to be caused by a CDF Roman Pot reinserting itself back into the beam after it had been issued retract commands. The Roman Pot motion control hardware has since then been found to be faulty. This event prompted an investigation in order to describe the sequence of events to understand the damage imposed on the collimator devices. Analysis of the quench data and collimator damage along with dynamic simulations of misbehaved beam, energy deposition and ablation process in the collimators, have provided with good agreement an explanation of the damage of Tevatron components. Fig. 1 shows the layout of the Tevatron and its Run II beam collimation system [1].
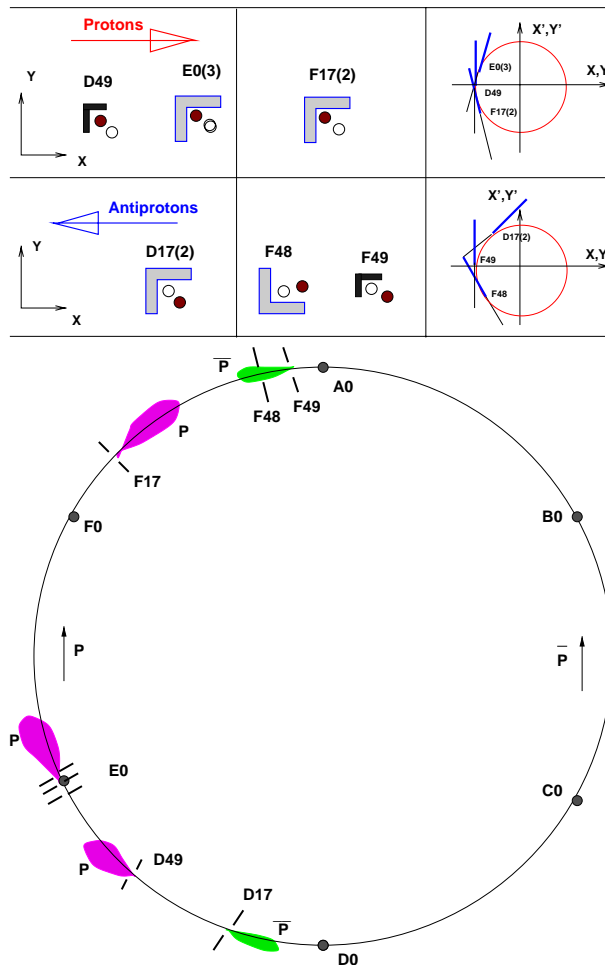

Figure 1: Tevatron layout and its Run II beam collimation system.

2   Sequence of Events that Led to Damage

The sequence of events that led to the 16 house quench and damage to the collimators and cryogenic spool piece is described in this section.

Event 1. Machine studies were planned at the end of the colliding beam store in order to commission a newly installed beam collimator at A48. Before the commissioning could begin, the CDF Roman Pots were required to be retracted out of the beam so that the pot detectors would not be damaged due to potentially increased losses during this study. The collimator and pot are only 0.5m from each other. Upon retraction of the pot, the pot reinserted itself back into beam due to a failure in motion control hardware. Later recreation of the failure suggests a velocity exceeding 1200 mills/sec or 0.03 mm/msec. The pot interacted with the proton and antiproton beams causing large losses at A48 and around the Tevatron ring (Fig. 2). When the pots were retracted, it appeared that not all of them had moved. Subsequent inspection showed that Pot-1 had an LVDT (a linear voltage differential transformer which translates a mechanical differential position to an electrical reading) that occasionally would stick when moving in the *OUT* direction. It cannot be verified but it is suspected that this LVDT incorrectly reported that Pot-1 was not fully retracted, causing the file to be manually sent again in an attempt to move it.

Event 2. Sending the retract file a second time caused the pots to move an additional distance past the desired park position until they contacted their limit switches. Pot-3 then entered its failure mode and ran back inward at high speed. A fraction of the beam interacted with the moving pot, creating a spray of particles towards the first downstream superconducting cell.

Event 3. The A48U cell (location of the Roman Pot) quenches immediately roughly 14 msec before the Tevatron abort fired. This can be seen in Fig. 3 which is a plot of the A4, D4, E1 and F1 Quench Protection Monitor (QPM) over sample buffer. These quenches are very fast and quench a large portion of the superconducting bus. The five main bus dipoles of the A48U cell begin to loose current at a conservative estimated rate of $\Delta I/\Delta t = 100$ V / 0.232 H = 431 A/sec, creating a distortion in the Tevatron horizontal orbit.
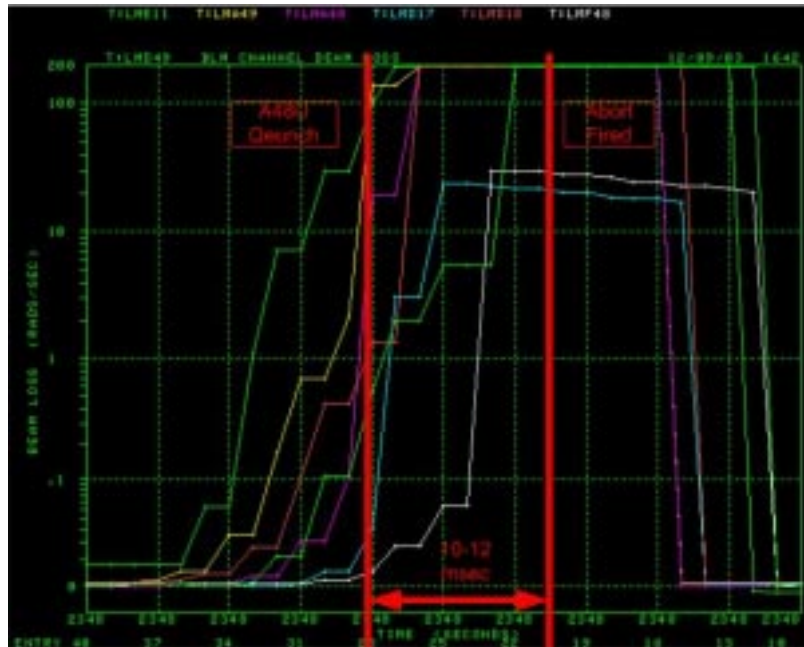

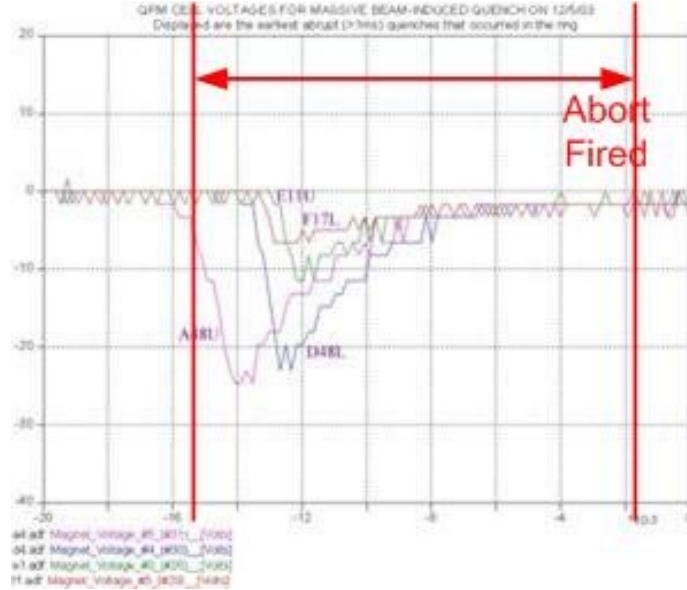Figure 2: Beam loss plot at various locations during the 16 house quench.

Figure 3: Voltage plots from QPMs over sample buffer depicting quenches at A4, D4, E1 and F1.

Event 4. Once the current began to decay in these five dipole magnets in the A48U cell (Fig. 4), the beam orbit began to change around the ring. The proton orbit at D49 began to move toward the D49 horizontal primary collimator radially inside at a rate of 0.36 mm/msec.
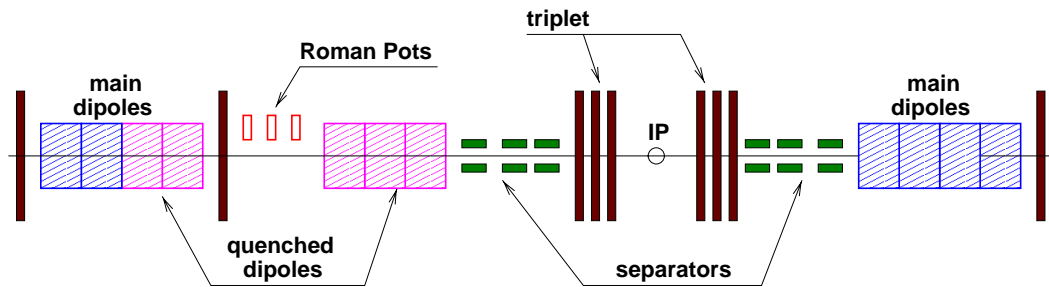
$$\frac{dI}{dt} = 500 \text{ A/sec} \implies \frac{dB}{B_O} = 2.39 \times 10^{-6} \text{ per turn}$$

Figure 4: Schematics of the BØ interaction region with its Roman Pots and quenching cell A48U.

Event 5. At the point when the primary proton beam reaches the D49 tungsten primary collimator (target) edge, it is estimated that in about 100-300 turns the beam would drill a semi-conical groove in the 5 mm tungsten wing and continue to circulate once a hole was created. This is a 5-mm thick tungsten wing used to scatter protons as part of a 2-stage collimation system for halo removal in the CDF and DØ experiments. Damage of the D49 target is shown in Fig. 5. Size of the exit hole at maximum is 2.8 mm. Note that, tungsten melting point is 3400 $^{\circ}C$.

Event 6. Once the hole in the D49 target was created, proton beam could travel to the next limiting horizontal aperture which would be the EØ3 1.5-m long stainless steel collimator. The beam then etched a horizontal groove in the collimator's vertical jaw (Fig. 6). This is a secondary collimator downstream of the D49 target to catch outscattered protons from the target. The groove in EØ3 is about 25 cm long and 1.5 mm deep.

Event 7. The abort system then fired the AØ abort kickers some 12-16 msec after the quench of A48U at which time there is no evidence that any beam – proton or antiproton – ending up at the abort blocks at AØ.
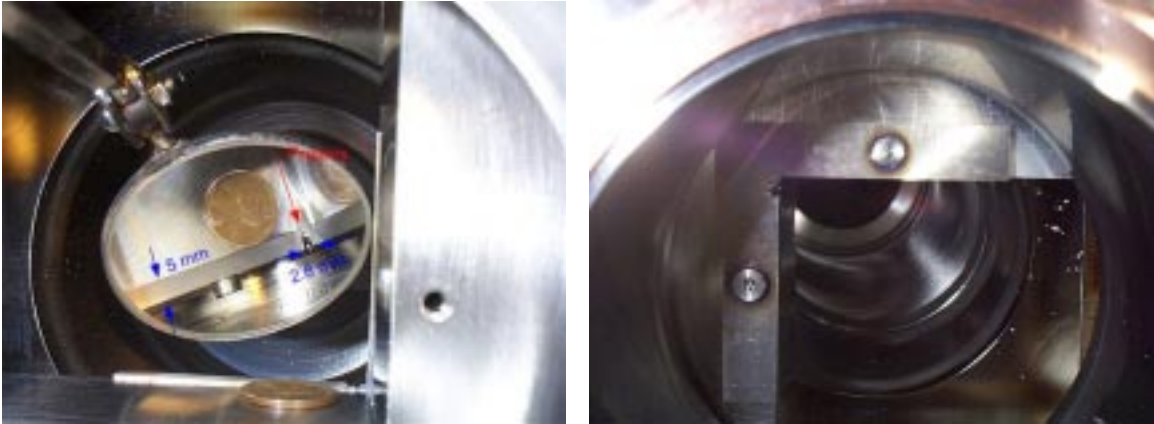

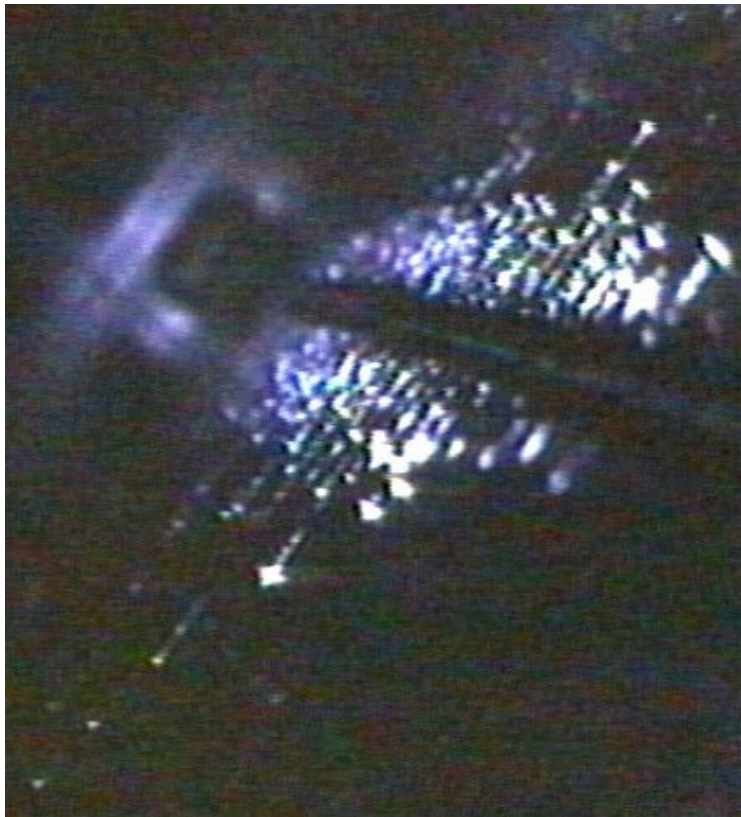Figure 5: Damage to D49 5-mm thick tungsten primary collimator.

Figure 6: Damage to EØ3 1.5-m long stainless steel collimator during the 16 house quench.

3 Beam Interaction with the CDF Roman Pot

The proton beam interaction with the A48 Roman Pot, rapidly moving into the circulating beam, was simulated to estimate the consequences of such an event. The Roman Pot cross section is shown in Fig. 7. In simulations, the Roman Pot consists of a 15 mm-thick scintillator contained in a 0.5 mm-thick stainless steel vessel. Protons interact with the vessel at the entrance and exit of the detector as well as along the beam side of whole device. At normal operation the Roman Pot is moved to working position at 8-10σ_x with a rate of 30 mm per second. In the simulations it was assumed that the Roman Pot crosses the aperture an order of magnitude faster. At these conditions the beam crosses a vessel beam-side wall with a velocity of 6.3 $\mu m/turn$. Even at this velocity most of the circulating beam interacts with beam-side wall, passing it twice on average. Lost proton vertical profile and time distribution in the wall are shown in Fig. 8. All protons are lost during 400 turns ($\sim$ 8.4 ms) starting from the beginning of beam interaction with the Roman Pot container. 48% of particles are lost in the Roman Pot beam-side wall, 30% – on the EØ3 collimator, 9% – on the F17(2) collimator, 3% – on the D49 collimator, and the rest are lost somewhere else on the Tevatron beam pipe. An estimation shows that the Roman Pot beam-side stainless steel wall melts under these conditions. As in reality, the A48 Roman Pot was not damaged during the December accident, it indicates that this scenario did not occur.
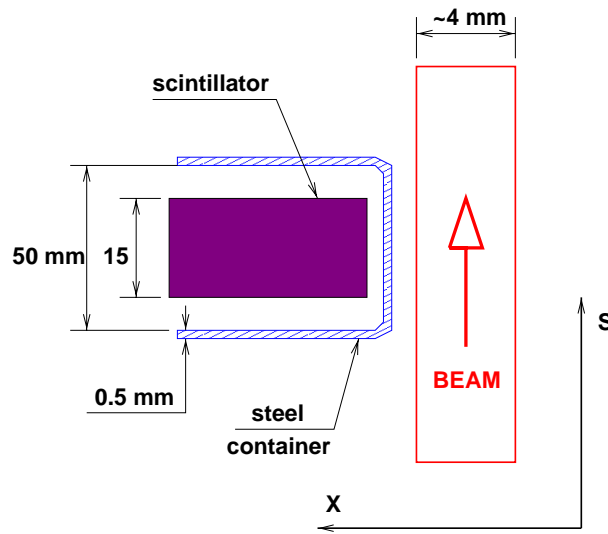

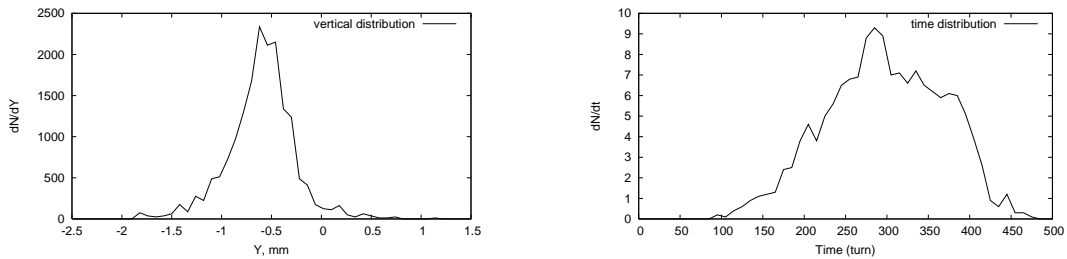Figure 7: Schematic view of the A48 Roman Pot and proton beam.

Figure 8: Lost proton vertical profile and time distribution in the A48 Roman Pot beam-side wall.

4   Beam Dynamics at Magnet Cell Quench

Normally, the beam scraping is done by the primary collimators at $5\sigma_{x,y}$ and secondary ones at $7\sigma_{x,y}$ at the beginning of accelerator cycle flat top after beams are brought to collisions. After the scraping is done, all collimators are retracted back from the beam by 1 mm, which is approximately equal to $2\sigma_{x,y}$. The slow proton beam halo growth in the Tevatron due to beam-gas interactions, intra-beam scattering, proton-antiproton collisions in the interaction regions (IP), and particle diffusion due to RF noise, ground motion and resonances excited by the accelerator magnet nonlinearities and power supplies ripple takes place at an average rate of about 3×10^7 p/s and the collimation system is designed to intercept 99.9% of this halo [1, 2]. After the collimators are retracted, the primary halo builds up to $7\sigma_{x,y}$ and secondary halo to $9\sigma_{x,y}$ during about 70 seconds with a number of protons above $5\sigma_{x,y}$ of about 2×10^9. In calculations below we assume that the number of protons outside $6\sigma_{x,y}$ is 5×10^8.

The analysis of this accident has shown that the Roman Pot moving fast towards the beam stopped at 5 mm from the beam pipe center (Fig. 9). The Roman Pot vessel was at $\sim6\sigma_x$ from the beam center. If the Roman Pot moved with a rate of 30 mm per second, it intercepted 5×10^8 protons during 15 msec, producing a tremendous spray of secondaries in the downstream magnets. This caused quench of the A48 superconducting magnet cell (Fig. 4). The magnet current degradation at the quench was equal to about 500 A/s. This gave a degradation rate of magnetic field in five dipole magnets of $\delta B/B_o = 2.39\times10^{-6}$ per turn. This process was simulated using the STRUCT code [3].

Fig. 10 shows proton and antiproton beam positions with respect to the collimator jaws. As shown in its bottom right, the circulating beam moves towards the D49 collimator jaw with a rate of ~0.005 mm per turn, and reaches the jaw surface by its 3σ-amplitude particles in approximately 300 turns after the quench start.

Proton hits at the collimators and the spill time distribution are shown in Fig. 11. The proton orbits at the Roman Pot and collimator locations are shown in Fig. 12 for turns number 200, 500 and 800 after the quench. The entire beam is lost during about 400 turns (8.4 msec) starting from turn number 400, mostly on the D49 primary collimator and EØ3 and F17(2) secondary collimators.
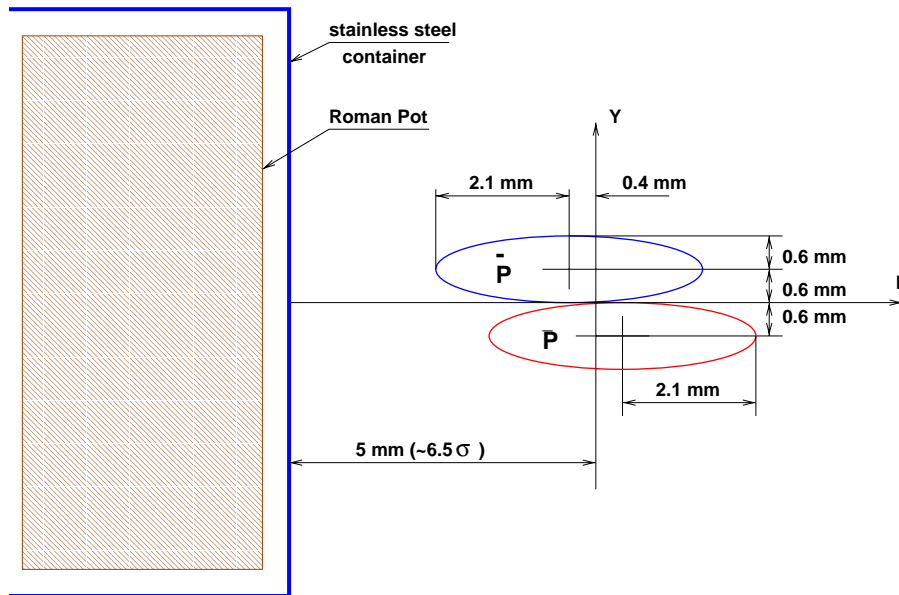

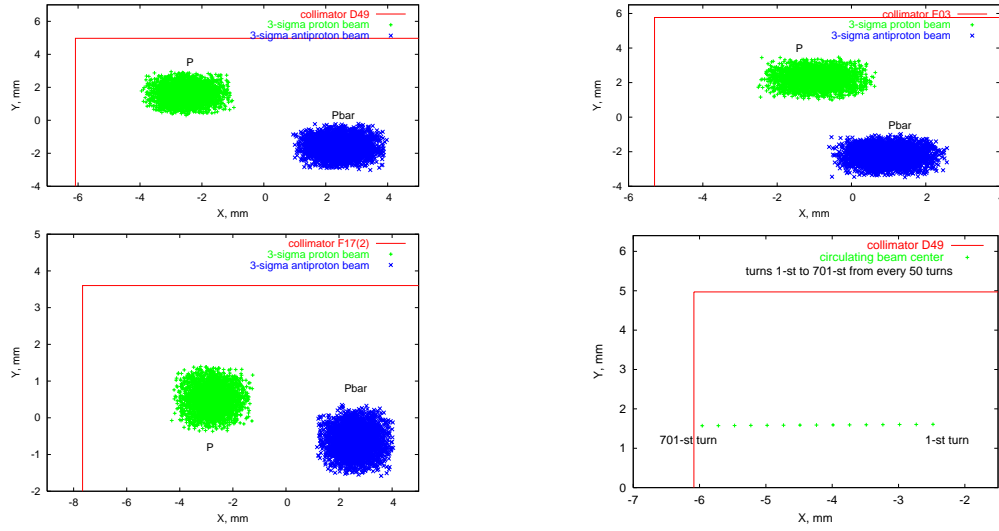Figure 9: Roman Pot detector position at accident.

Figure 10: The 3-σ proton and antiproton beams at the proton collimators and proton beam orbit position with respect to the D49 collimator jaws at the A48 cell quench (bottom-right).
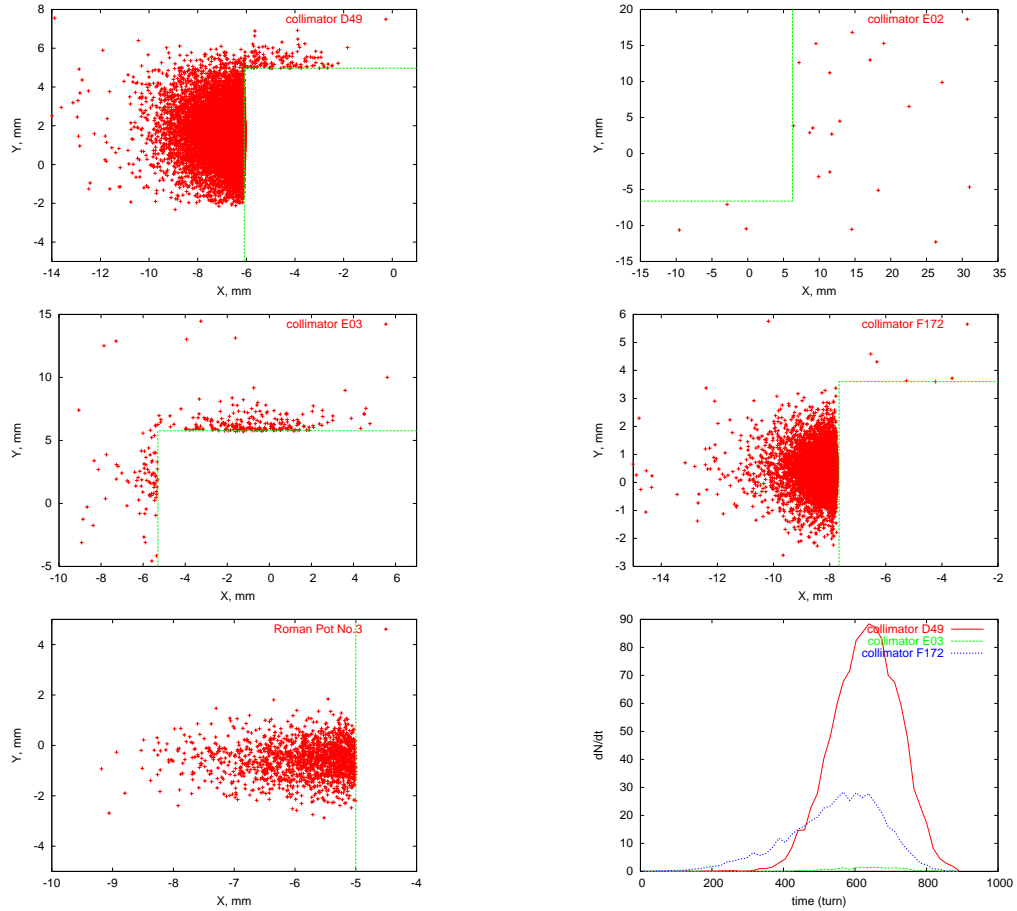

Figure 11: Proton hits on the collimators D49, EØ2, EØ3, F172 and at Roman Pot at dynamic simulations of the A48 dipole cell quench. A time distribution of hits is shown on bottom-right of the figure. Collimators are retracted from their working positions by 1 mm.
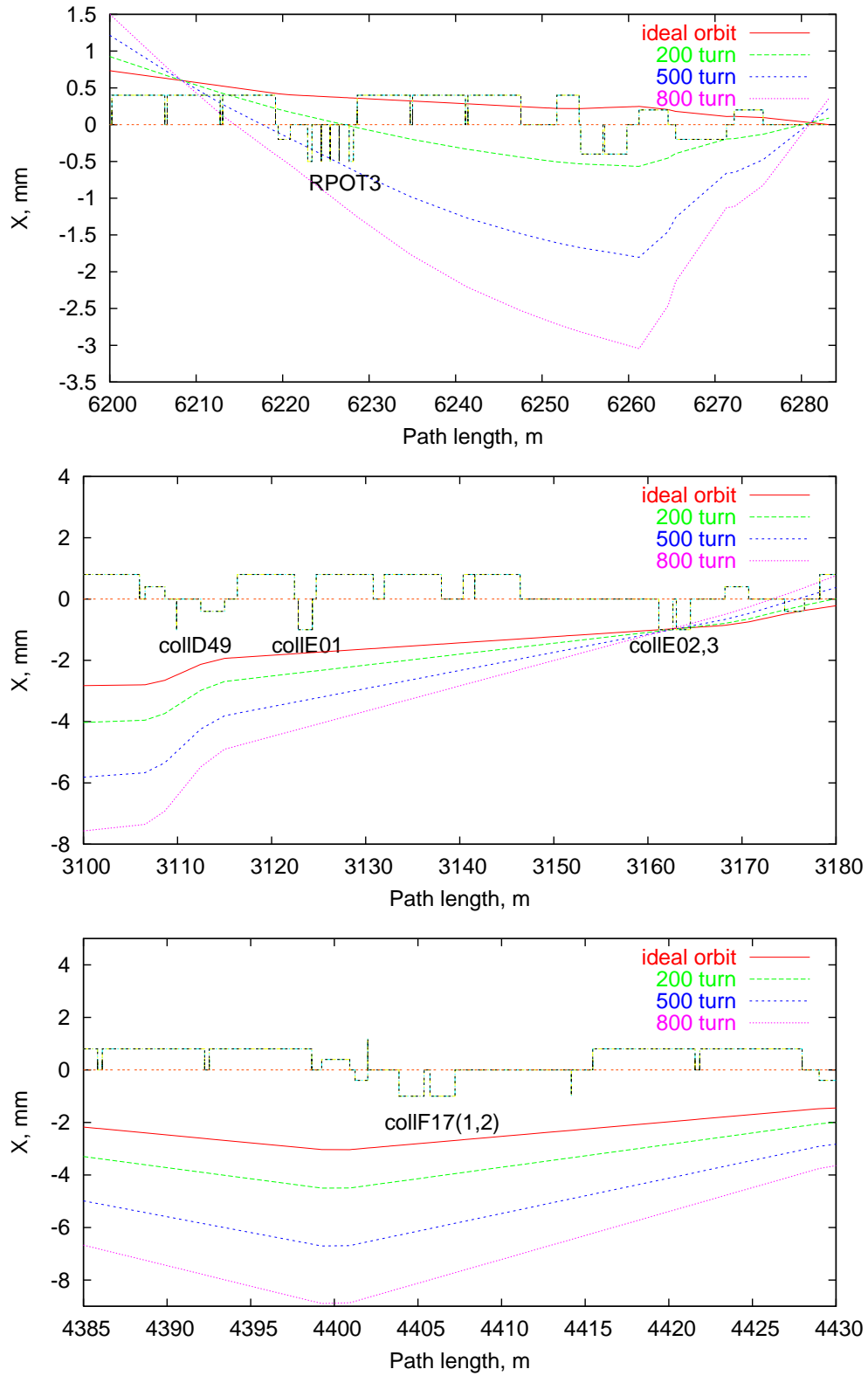
Figure 12: Ideal proton beam orbit and orbit at turn No. 200, 500 and 800 at the quench of five main dipoles in the A48 region.

A fraction of the beam loss in the collimators depends on the collimator F17(2) position with respect to the beam. As mentioned above, after the scraping is done, all the collimators are normally retracted back from the beam by 1 mm. The collimator F17(2) is retracted by 3 mm, because of a large dispersion at this location. As shown in Fig. 13 this increases beam loss in the collimator EØ3 and decreases losses in the collimator F17(2).
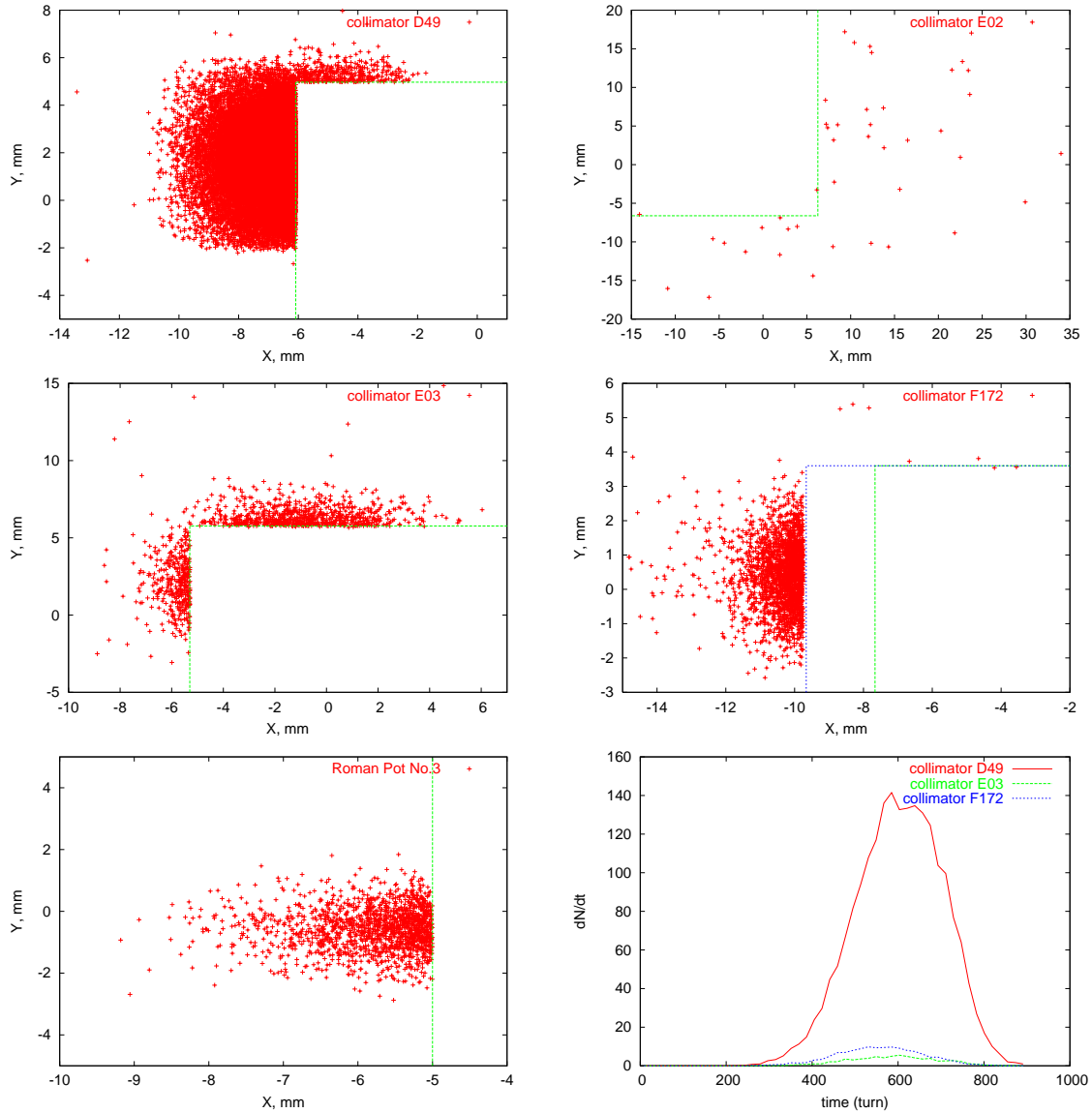

Figure 13: Proton hits on the collimators D49, EØ2, EØ3, F172 and Roman Pot at dynamic simulations of the A48 dipole cell quench. A time distribution of hits is shown on bottom-right of the figure. The horizontal collimator F17(2) is retracted from the working position by 3 mm, all others are retracted by 1 mm.

10

5 Energy Deposition in Collimators

Using the beam loss distributions calculated in the previous section for the A48 magnet cell quench, detailed energy deposition modeling was performed with the MARS14 Monte Carlo code [4] for the D49 primary, and F17(2) and EØ3 secondary collimators. Here we assume that the energy deposition process in the collimators starts after the 500th turn or 10 ms after the beginning of quench development, with majority of particles lost over 50 turns or 1 ms. Fig. 14 shows two-dimensional contours of energy deposition density in a 0.5-mm layer of the tungsten vertical jaw of a L-shaped D49 primary collimator. One sees that energy deposition is noticeably larger at the downstream end of a 5-mm plate, because of an intense cascade development for a 980-GeV proton beam over 1.5 radiation length thickness. Transverse profiles of energy deposition at the upstream and downstream ends of the plate are shown in Fig. 15. One can expect that a semi-conical groove is drilled in the vertical jaw shown in black in the figures (roughly above 300 J/g), that is confirmed in next Section. The hole diameter at the downstream end is about 2.5-3 mm.
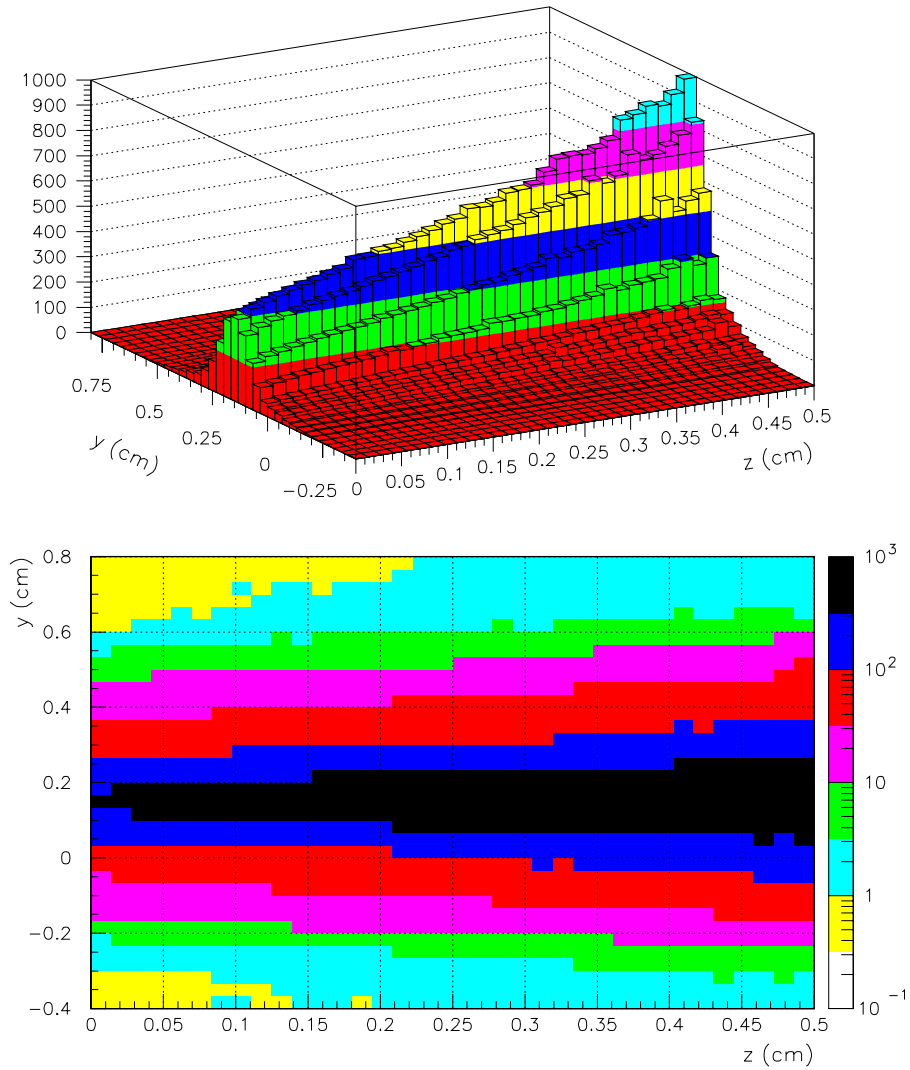
ED (J/g), TeV 12/05/03 Accident − D49 W (−x=0.6085−0.6585 cm) MARS14 01/16/04

Figure 14: Energy deposition isocontours along the beam in the D49 tungsten vertical jaw.
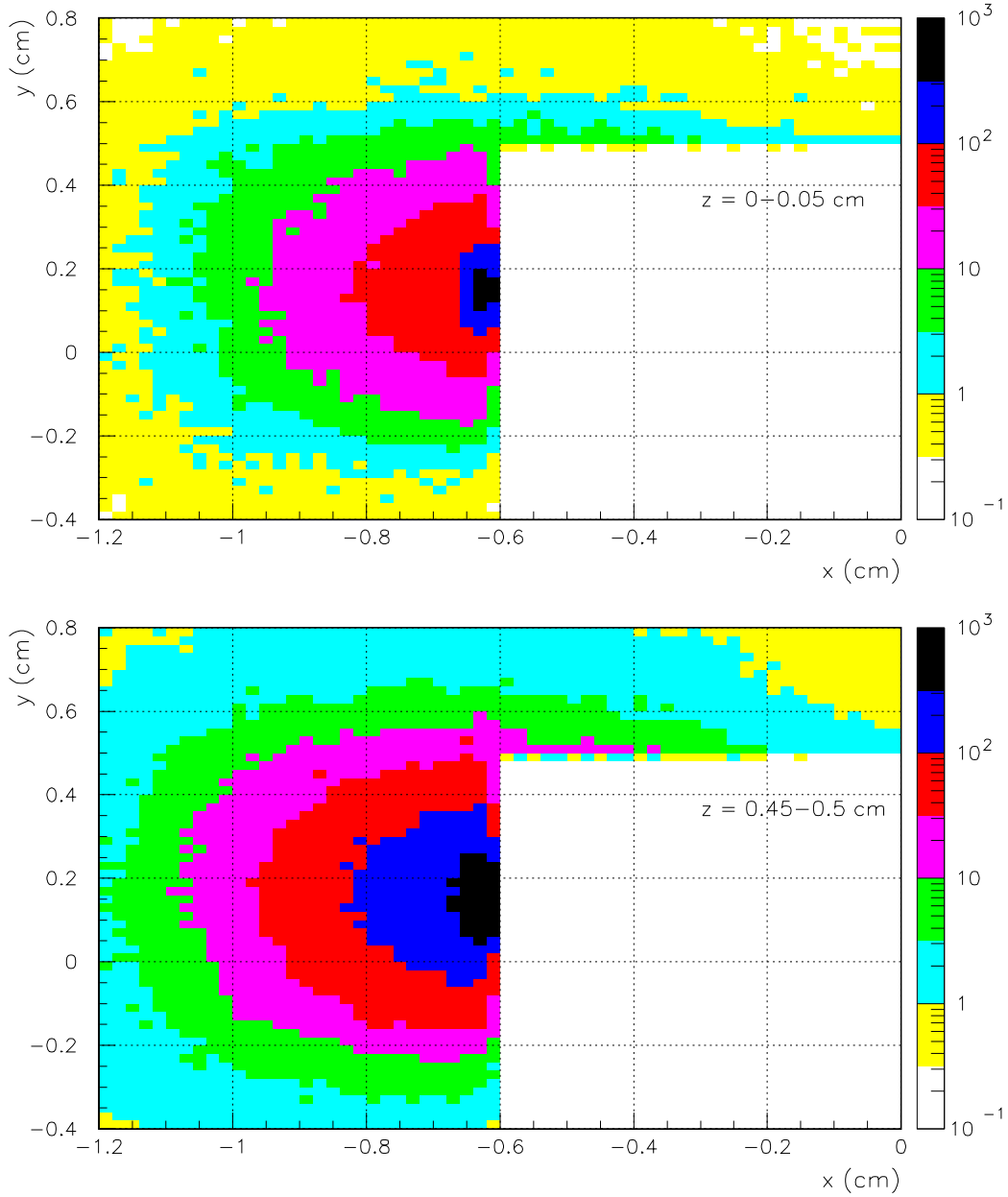
ED (J/g), TeV 12/05/03 Accident – D49 W MARS14 01/16/04

Figure 15: Energy deposition isocontours in the transverse slices at the upstream and downstream ends of the D49 tungsten jaws.

Stainless steel jaws of the secondary collimators F17(2) and EØ3 can also be severely damaged by the misbehaved beam. Using the proton distributions shown in Fig. 13, full-scale energy deposition calculations were again performed with the MARS14 for 1.5-m long L-shaped jaws of those collimators. Fig. 16 shows two-dimensional contours of energy deposition density along the jaws in the beam-side layer and across the jaw at shower maximum (z=26 cm). One can expect that a 250-mm long and 3-mm wide slot is created in the collimator vertical jaw. Fig. 17 shows similar results for the EØ3 secondary collimator.
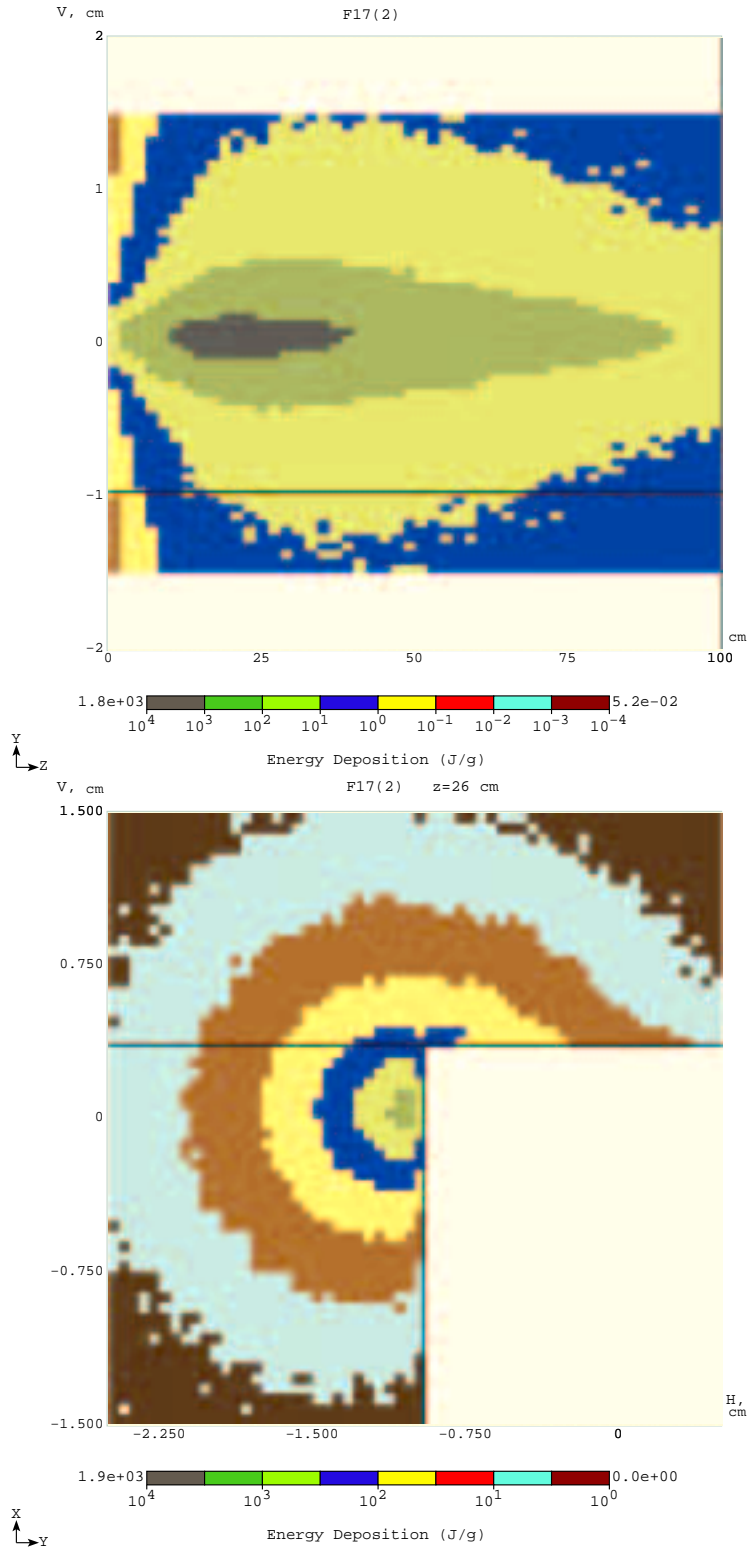
Figure 16: Energy deposition isocontours along the beam in the F17(2) stainless steel vertical jaw (top) and across the jaw at shower maximum (bottom).
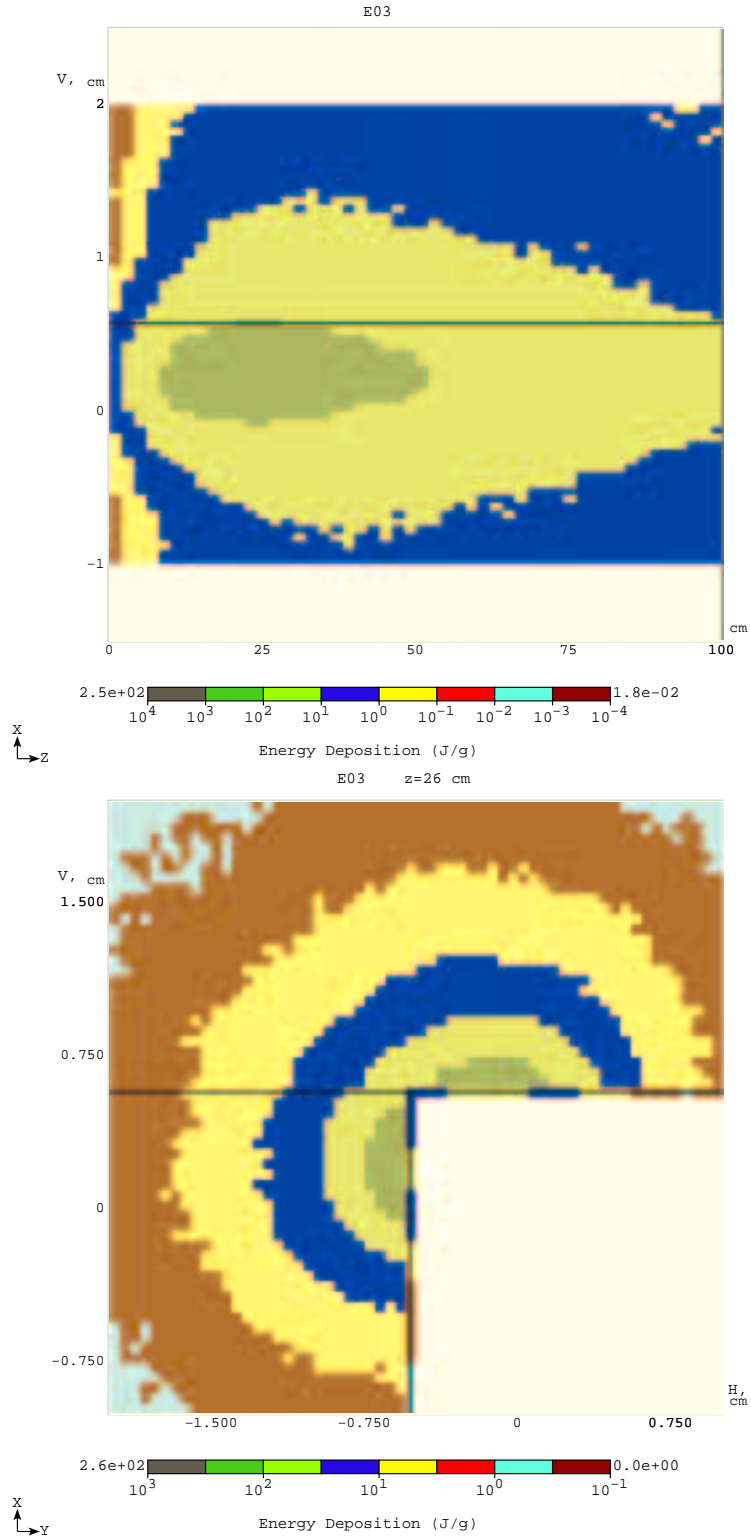
Figure 17: Energy deposition isocontours along the beam in the EØ3 stainless steel vertical jaw (top) and across the jaw at shower maximum (bottom).

6 Ablation of the Tungsten Collimator

The interaction of intense proton pulses with the collimator can result in rapid local heating and ablation of primary collimator tungsten or secondary collimator stainless steel from the surface. In this section a detailed consideration is given to the ablation process for D49 tungsten that takes place in high vacuum. It can not be approximated as a phase transition of equilibrium thermodynamics. We believe that the pressure of the ablated gaseous material and its influence on the return mass flow to the solid surface was negligible especially at initial stages of ablation. Therefore, following a standard approach in surface physics [5, 6], we define the desorption rate, or the number of atoms leaving the unit surface of the solid tungsten in unit time, as

$$dN = N_0 \nu e^{-E_D/kT},\tag{1}$$

where N_0 is the number of atoms on the unit surface, $\nu = 10^{13}\,\mathrm{sec}^{-1}$, and E_D is the surface energy per tungsten atom which is equal to the heat of vaporization per atom, k is the Boltzmann constant, and T is the absolute temperature. The tungsten heat of vaporization is $Q_v = 824\,\mathrm{kJ/mol} = 1.3683 \cdot 10^{22}\,\mathrm{J/atom}$ and $N_0 = \sqrt{2}/a^2$, where a is the lattice constant; for tungsten $a = 3.16$ Å.

The equation for the evolution of temperature in the collimator plate is

$$\frac{dT}{dt} = \frac{1}{C_p}\frac{dE_\mathrm{ext}}{dt} + \kappa\nabla T,\tag{2}$$

where C_p is the specific heat at constant pressure, κ is the heat conductivity, and E_ext is the external energy deposited by the proton beam and calculated numerically using the MARS14 code.

Therefore, solving (2) and using (1), the normal displacement due to ablation of a surface element during time dt can be calculated as

$$dl = \frac{m_0 N_0 \nu dt}{\rho} e^{-Q_v/kT},\tag{3}$$

where the tungsten density $\rho = 19.35\,\mathrm{g/cm}^3$, and the atomic mass $m_0 = 183.85\,\mathrm{au} = 3.053\cdot 10^{-22}\,\mathrm{g}$.

We have developed the following numerical scheme to study the process of ablation of the tungsten collimator plate. The clock in this scheme starts at the 500th turn or 10 ms after the beginning of quench development, with protons responsible for damaging energy deposition lost over 50 turns or 1 ms. At every time step, we calculate the energy deposition in the material by interpolating the tabulated data set which was obtained in the previous section using the MARS14 code. We use smooth polynomial interpolation in interior points, and linear extrapolation for points which are outside the MARS data file. We find the temperature distribution in the plate by integrating equation (2). Then, the normal propagation of the front and back surfaces is calculated using (3). The new location of the surfaces is then interpolated to the rectangular grid using smooth polynomial interpolation. The calculation of the energy deposition for the next time step accounts for the reduction of the plate thickness due to ablation.

Numerical simulation results are given in Fig. 18. It shows the time evolution of the front and back surfaces of the D49 collimator plate. We observe that the ablation of the back surface is much faster at early time due to the nature of the energy deposition by intensive proton beams. At later time, the ablation rates at two surfaces are approximately equal. One sees that the hole is created in 1 ms from the beginning of the process, i.e., at about 550th turn or 11 ms after the beginning of quench development. The shape of this hole at this moment is shown in bottom of the figure.

We note that the numerical results presented above give the fast time limit estimate of the ablation process. This is due to the fact that some processes which may slightly slow down the ablation

were neglected. These include the reduction of the internal energy of the collimator plate due to the kinetic and internal energy of the ablated material as the kinetic energy of the ablated material is unknown. A study based on quantum mechanics would be needed to estimate this energy. The pressure of the ablated gaseous material was also neglected which may contribute during late stages of the ablation. A study coupled to the gas expansion dynamics would be necessary to account for this phenomenon.
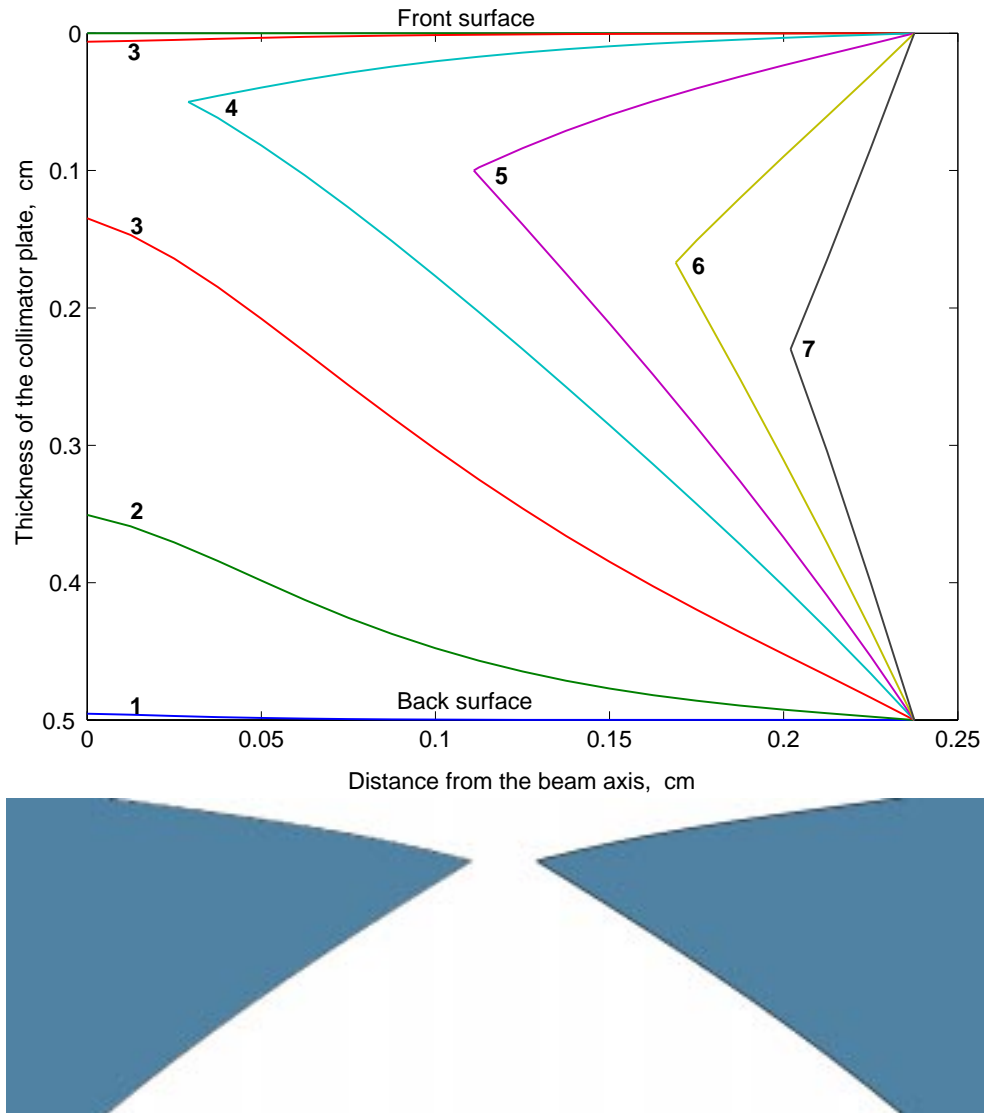

Figure 18: Top: evolution of the front and back surfaces of the tungsten collimator plate from t=0.4 ms (1) through t=1.6 ms (7) with Δt=0.2 ms. Bottom: shape of the hole in the collimator plate at 1 ms.

7 Beam Loss During Hole Creation

In this section, a rough estimate is made on dynamics of the beam lost during the ablation process in the D49 collimator. The ablation here was simulated by shifting out the jaw with a rate of 0.003 mm per turn starting the 550th turn. Accumulated hits at the collimators are shown in Fig. 19. Comparing to a undestructed jaw case (Fig. 13), one sees that the dynamic hole creation in the primary collimator reduces the total load and duration of loss on the D49 collimator producing a longer tale of loss on the secondary ones.

At normal operation and at the beginning of the accident, the halo particles interacting with the primary collimator produce a broad hit distribution at the secondary collimators with a relatively small density at the secondary jaw edge. At the accident, once a semi-conical groove was created in the primary collimator, the secondary collimators became the first limiting aperture for the halo with significant particle outscattering. This resulted in substantially increased radiation loads on the downstream equipment inducing the quench of several superconducting magnet cells downstream of F17 and E0.
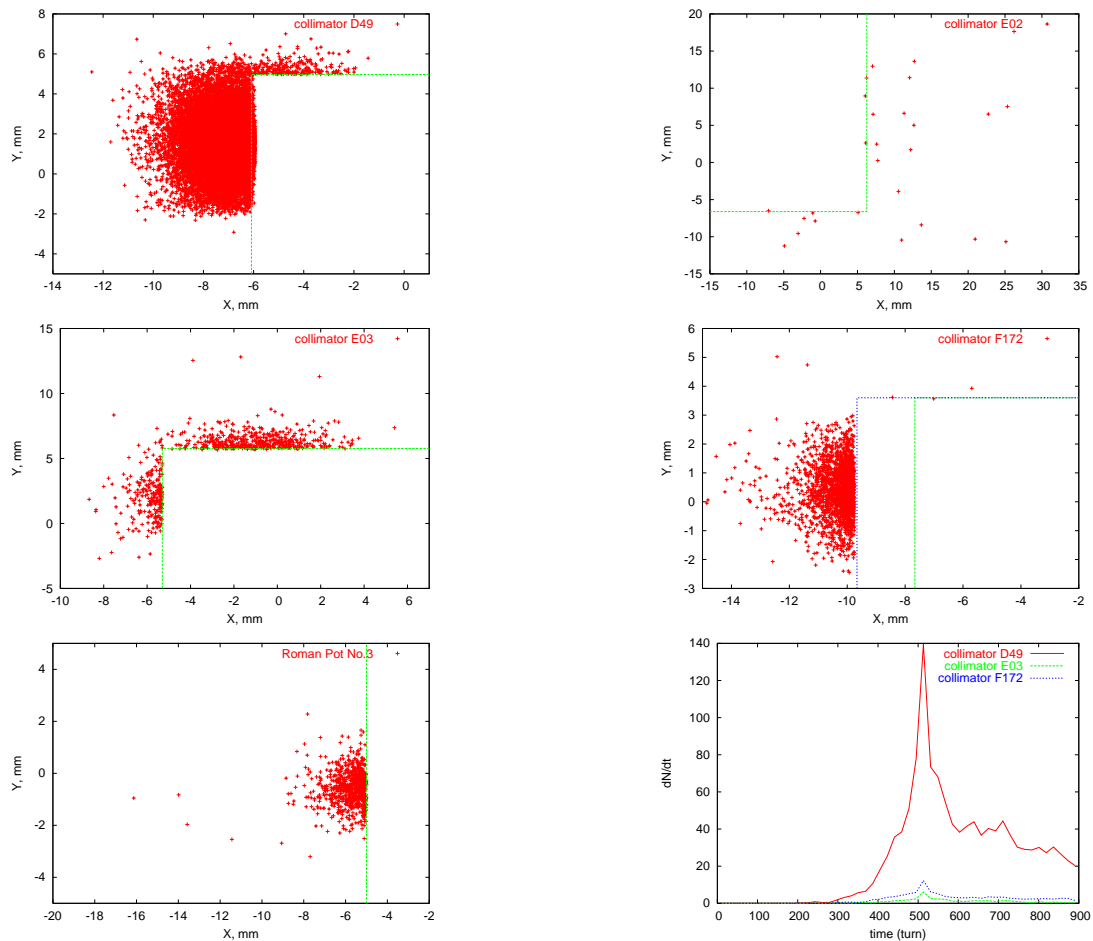

Figure 19: Proton hits on the collimators D49, EØ2, EØ3, F172 and Roman Pot at dynamic simulations of the A48 dipole cell quench. A time distribution of hits is shown on bottom-right of the figure.

8   Conclusions

Analysis and simulations performed show that we have a good understanding of the entire picture of the December 2003 beam accident, both on dynamics and material damage sides. Calculated parameters of the hole and groove created in the collimators are very similar to those observed after the accident. There is work in progress to eliminate a possibility for such an accident in future. The current Tevatron beam loss monitor (BLM) has the capability of triggering a beam abort on loss limits but operationally have found the system is not explicit enough and has resulted in colliding beam stores being lost due to false detection of losses. Therefore, currently during the Tevatron colliding beam stores, the BLM abort triggering capability is masked out in order to avoid aborting stores due to false indications. A new BLM system under consideration is to operate with multiple types of loss detection (average loss, fast and slow losses) and with independent abort threshold. The system will also have the capability to have different loss abort limits for different Tevatron states such as acceleration, injection and collisions.

9   Acknowledgments

References

[1] M.D. Church, A.I. Drozhdin, A. Legan, N.V. Mokhov, R.E. Reilly, "Tevatron Run-II Beam Collimation System" in *1999 Particle Accelerator Conf.*, IEEE Conference Proceedings, New York, 1999, pp. 56–58; Fermilab-Conf-99/059 (1999).

[2] A.I. Drozhdin, V.A. Lebedev, N.V. Mokhov, L.Y. Nicolas, D.V. Sidorov, S.I. Striganov, A.V. Tollestrup, "Beam Loss and Backgrounds in the CDF and DØ Detectors due to Nuclear Elastic Beam-Gas Scattering", Fermilab-FN-734 (2003).

[3] I.S. Baishev, A.I. Drozhdin, N.V. Mokhov, "STRUCT Program User's Reference Manual", SSCL–MAN–0034 (1994); http://www-ap.fnal.gov/∼drozhdin/

[4] N.V. Mokhov, "The MARS Code System User's Guide", Fermilab-FN-628 (1995); N.V. Mokhov, O.E. Krivosheev, "MARS Code Status", *Proc. Monte Carlo 2000 Conf., pp. 943-948*, Lisbon, October 23-26, 2000; Fermilab-Conf-00/181 (2000); N.V. Mokhov, "Status of MARS Code", Fermilab-Conf-03/053 (2003); http://www-ap.fnal.gov/MARS/.

[5] G. Iche, P. Nozieres, J. Phys. (Paris), **37** (1976), 1313.

[6] J. Davenport, G. Dienes, R. Johnson, Phys. Rev., **B25** (1982), 2165 - 2174.